RSC Advances

PAPER

View Article Online
View Journal | View Issue

Cite this: *RSC Adv.*, 2022, **12**, 32297

Multifunctional nanoprobes combined with radiotherapy and hypoxia-activated therapy synergistically improve antitumor efficacy†

Lingwei Wang, ‡[a] Mengyang Zhang,‡[a] Xujie Gao,[a] Jiang Li,[b] Menglin Wu,[b] Xuening Zhang *[b] and Zhaoxiang Ye*[a]

Received 27th July 2022
Accepted 25th October 2022

DOI: 10.1039/d2ra04690c

rsc.li/rsc-advances

The presence of hypoxia in tumors is characteristic of most solid tumors and it promotes not only tumor angiogenesis but also tumor cell invasion and metastasis. It also results in resistance of tumor tissue to radiation, leading to poor outcomes of tumor radiotherapy. Therefore, to address this conundrum, highly selective gold nanoclusters were prepared as fluorescent imaging agents and radiosensitizers and then loaded with tumor hypoxia-activated prodrugs to prepare nanoprobes which synergistically improved the anti-tumor efficacy by combining radiotherapy and hypoxia-activated therapy. The designed nanoprobes have ultra-small size, high selectivity for integrin $\alpha_v\beta_3$ receptor-positive tumor cells and tumor neovascular endothelial cells, and excellent fluorescence imaging performance. The experimental procedures were carried out *in vitro* and *in vivo* to demonstrate that the developed nanoprobes have a high level of biocompatibility, efficient radiosensitization effect, and anti-tumor efficacy at cell and tissue levels. The combined application of radiotherapy and hypoxia-activated therapy can overcome the radiation resistance caused by tumor hypoxia, compensate for the limitations of single radiotherapy, inhibit tumor growth, improve the efficacy of tumor radiotherapy, and provide new possibilities for the development of more precise and effective treatment strategies.

1. Introduction

Tumor hypoxia is a typical characteristic of solid tumors and plays a significant role in the progression of tumors and treatment resistance.[1–3] The harsh microenvironment of tumors, such as the accelerated growth of tumor cells and the imperfect formation and uneven distribution of tumor angiogenesis, leads to an insufficient oxygen supply in the tumor. A hypoxic microenvironment can activate the signaling pathway of hypoxia-inducible factor-1 (HIF-1), enhance the expression of genes such as vascular endothelial growth factor (VEGF), and result in tumor angiogenesis and tumor cell invasion and metastasis.[4–8] To address this conundrum, increasing the amount of oxygen, such as generating molecular oxygen by decomposing hydrogen peroxide, is suggested to treat the hypoxia existing in the tumor microenvironment.[9,10] This can help reduce symptoms of tumor hypoxia. Compared with anti-hypoxia, using tumor hypoxia to improve tumor therapy, such as the application of hypoxia-activated prodrugs, has attracted great recent research interest.[11,12] Under hypoxic conditions, hypoxia-activated prodrugs can be reduced to therapeutic drugs by various intracellular reductases, such as AQ4N, a novel bioreductive drug that can be reduced to cytotoxic AQ4 under hypoxic conditions, thereby selectively killing tumor hypoxic cells.[13–16] However, applying hypoxia-activated prodrugs alone usually cannot achieve satisfactory antitumor effects due to their ineffectiveness against tumor cells with sufficient oxygen supply near tumor blood vessels. Traditional tumor treatments, such as radiotherapy, preferentially target well-oxygenated regions of the tumor and have a limited effect on poorly vascularized hypoxic regions due to the need for oxygen to generate DNA-damaging cytotoxic free radicals during radiotherapy.[17–20] When the oxygen concentration is less than 20 mmHg, the tumor is resistant to conventional radiotherapy, resulting in a poor prognosis of tumor radiotherapy.[21] Therefore, the combined application of radiotherapy and hypoxia-activated therapy can make up for the limitations of radiotherapy or hypoxia-activated therapy alone and is an ideal strategy to utilize tumor hypoxia to enhance the anti-tumor effect. Gold nanoclusters (AuNCs) are relatively stable nanostructures composed of several to hundreds of gold atoms, usually 1–10 nm in size, which can produce an aggregation-induced emission (AIE) effect, resulting in stable fluorescence.[22–25] As

[a]*Tianjin Medical University Cancer Institute & Hospital, National Clinical Research Center for Cancer, Tianjin's Clinical Research Center for Cancer, Key Laboratory of Cancer Prevention and Therapy, Tianjin, PR China. E-mail: zye@tmu.edu.cn*

[b]*Department of Radiology, Second Hospital of Tianjin Medical University, Tianjin, PR China. E-mail: luckyxn@126.com*

† Electronic supplementary information (ESI) available. See DOI: https://doi.org/10.1039/d2ra04690c

‡ Lingwei Wang and Mengyang Zhang contributed equally to this work.

a high-atomic-number (high-*Z*) element, gold can generate additional reactive oxygen species (ROS) in the enriched area of the tumor after radiation therapy, improving the sensitivity of the tumor to radiation and the efficacy of radiotherapy.[26,27] According to the findings of several research works, the relative radiosensitization level of gold nanoparticles significantly increases as the particle size of nanoparticles decreases.[28,29] Therefore, benefiting from their unique structure and ultra-small size, gold nanoclusters can be applied as fluorescent imaging agents and radiosensitizers. However, severe reticulo-endothelial system (RES) capture, rather than efficient tumor targeting, resulted in most nanoparticles not performing as originally designed for *in vivo* applications.[30,31] Integrins are a class of cell surface receptors that mediate recognition and adhesion between cells and the extracellular matrix.[32] Studies have revealed that integrin receptors, such as $\alpha_v\beta_3$, a specific proteins on the surface of tumor cells and tumor neovascular endothelial cells, are potential candidate for targeted drug delivery.[33] RGD sequence, composed of arginine, glycine, and aspartic acid, is the recognition site for the interaction between integrin receptors and ligand proteins and exhibits a high binding capacity to $\alpha_v\beta_3$.[34,35] Therefore, nanocarriers modified with polypeptides containing RGD sequences can effectively improve the selectivity of tumor cells and tumor neovascular endothelial cells, improve the efficiency of drug delivery, and reduce side effects on normal tissues.

In this study, fluorescent RGDfC-AuNCs were prepared by the biomineralization method using peptides containing RGD sequence as templates and then loaded with the hypoxia-activated prodrug AQ4N to prepare AQ4N@AuNCs. As displayed in Fig. 1, when the nanoprobes were injected into mice, the surface-coated RGD sequences could be specifically attached to different receptors, integrin, found on the surface of tumor cells and tumor neovascular endothelial cells, thus promoting the nanoprobes into tumor tissue. After radiotherapy, RGDfC-AuNCs may boost the radiosensitization effect of normoxic tumor cells at low radiation doses, and then the nanoprobe-loaded hypoxia-activated prodrug AQ4N can be reduced to cytotoxic AQ4 in hypoxic tumor cells, thereby selectively killing hypoxic tumor cells.

2. Methods

2.1 Materials

All chemicals were obtained commercially without further purification. The cRGDfC (cyclo Arg–Gly–Asp–D-Phe–Cys, MW = 578.66) peptide was purchased from GL Biochem Co., Ltd. Glutathione (GSH) was obtained from Solarbio. Chloroauric acid ($HAuCl_4$) was supplied by Sigma-Aldrich. Banoxantrone (AQ4N) was acquired through GlpBio. From Gibco BRL, we obtained Dulbecco's Modified Eagle's Medium (DMEM) and Fetal Bovine Serum (FBS). CCK8 was provided by Precision BioMedicals Co., Ltd. Cleaved-caspase 3 antibody and gamma-H2AX antibody were purchased from Abcam.

2.2 Synthesis and characterization of AQ4N@AuNCs

The synthesis of fluorescent RGDfC-AuNCs followed a previously reported protocol.[36] Aqueous $HAuCl_4$ solution (24 mM, 50 μL) was applied to a solution of cRGDfC peptide (1 mg mL^{-1}, 2 mL) with vigorous shaking, and then a solution of NaOH (0.5 M, 50 μL) was used to adjust the pH of the solution between 12 and

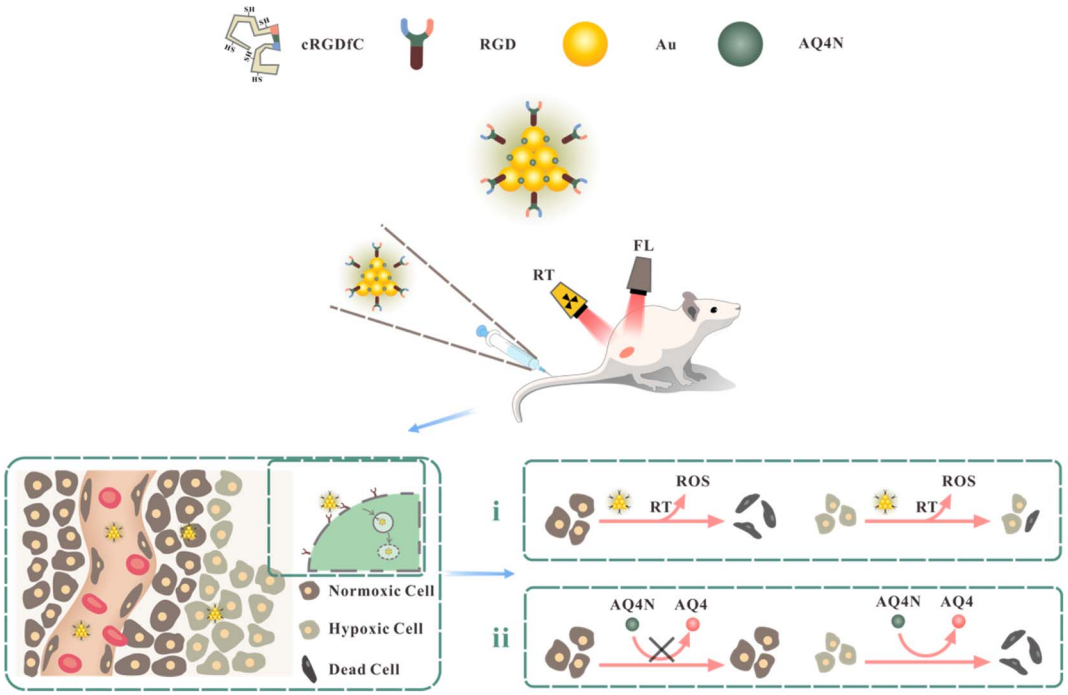

Fig. 1 Schematic representation of AQ4N@AuNCs in synergistic radiotherapy and hypoxia-activated therapy *in vivo*.

14. The mixture was warmed to a temperature of 50 °C, and the process proceeded for 24 hours. Following the reaction, the mixture was filtered using ultrafiltration centrifuge tubes (3 KD) to remove the free cRGDfC peptide. To synthesize AQ4N@AuNCs, AQ4N solution (1 mg mL^{-1}) and RGDfC-AuNCs solution (1 mg mL^{-1}) were combined using a mass-to-volume ratio of 1 : 4 and then rapidly shaken at room temperature for 24 hours. Following the reaction completion, the mixture was purified with ultrafiltration centrifuge tubes (3 kD) to get rid of any free AQ4N, and then it was kept at 4 °C for later use.

Transmission electron microscopy (JEOL JEM-2100F) was utilized to identify the shape, particle size, and dispersibility. The UV-spectrophotometer (Shimadzu UV-1700) was utilized to determine UV-Vis absorption spectra. The spectrofluorophotometer (Shimadzu RF-6000) was employed to calculate the excitation and emission spectra. By using dynamic light scattering (Malvern ZS90), we determined the hydrated particle size and the zeta potential. *In vitro* fluorescence imaging performance was measured by IVIS Lumina Series III.

2.3 *In vitro* cytotoxicity of AQ4N@AuNCs

CCK8 assay was utilized to determine the viability of 4T1 cells treated with AQ4N@AuNCs. At 37 °C and 5% CO_2, 4T1 cells were incubated in 96-well plates at 5×10^3 cells per well for 24 hours in DMEM media with 10% FBS. Then, 10 μL of AQ4N@AuNCs solutions at different concentrations (final concentrations of 25, 50, 100, 200, 400, and 800 μg mL^{-1}) were applied to every well, followed by 24 hours of incubation. The media was drained and rinsed with phosphate-buffered saline (PBS) after incubation and replaced with fresh DMEM media. CCK8 (5 mg mL^{-1}, 10 μL) was applied to every well, and the incubation continued for 2 hours. Lastly, absorbance at 450 nm was calculated for each well by a microplate reader. The equation for calculating cell viability is as follows:

$$\text{cell viability } (100\%) = \text{mean absorbance of} \frac{\text{treatment group}}{\text{control group}}.$$

2.4 *In vitro* cellular uptake of AQ4N@AuNCs

The uptake of AQ4N@AuNCs by cells was observed using a confocal laser scanning microscope (CLSM). A549 and MCF-7 cells were cultivated in 6-well plates with 5×10^4 cells for every well with 5% CO_2 and 37 °C in DMEM medium with 10% FBS for 24 hours. Then, 10 μL of a mixture having the fluorescent dye Cy5-labeled AQ4N@AuNCs (final concentration of 600 μg mL^{-1}) was applied to every well, followed by 8 hours incubation. Following incubation, the samples were rinsed with PBS, fixed with paraformaldehyde (4%), and dyed with 4′,6-diamidino-2-phenylindole (DAPI). Lastly, the samples were studied using CLSM under Cy5 channel (excitation 649 nm, emission 669 nm).

2.5 *In vitro* synergistic therapy of AQ4N@AuNCs

To evaluate the synergistic therapeutic effect *in vitro*, 4T1 cells were pretreated with cobaltous chloride ($CoCl_2$) for hypoxia, and the cell viability of 4T1 cells treated with AQ4N@AuNCs under radiation or non-radiation conditions was detected by CCK8 assay. 4T1 cells were incubated at 5×10^3 cells in every well in 96-well plates for 24 hours, followed by the addition of 10 μL of $CoCl_2$ per well to a final concentration of 100 μmoL L^{-1} and continued incubation for 24 hours. Then, AQ4N@AuNCs solution was added to make a final concentration of 800 μg mL^{-1}, the incubation was continued for 8 hours, and PBS was added as blank control. After the incubation, excess AQ4N@AuNCs were removed by washing with PBS and irradiated with an 8 Gy X-ray, while the incubation lasted for 16 hours. At last, 4T1 cell viability was determined using CCK8 assay. To assess the radiosensitization effect *in vitro*, AQ4N@AuNCs solution and CMNa solution were added to make a final concentration of 800 μg mL^{-1}, followed by X-ray irradiation of 0 (control), 2, 4, 6, and 8 Gy, respectively, and the cell viability was detected.

2.6 Animal and tumor model

All animal experiments were conducted in accordance with protocols approved by the Animal Care and Use Committee of the Cancer Institute and Hospital of Tianjin Medical University. The Beijing Vital River Laboratory Animal Technology Co., Ltd. supplied female BALB/c mice (4–6 weeks, 20 g). To create 4T1 tumor model, every mouse was injected in the right thigh with a 4T1 cell suspension (5×10^6 cells dispersed in 100 μL PBS). When the tumor volume reached about 100 mm^3, 4T1 tumor model was effectively generated after daily observation of the tumor's progression. The calculation formula of tumor volume is as follows:

$$\text{tumor volume } (V) = \frac{\text{length } (L) \times \text{width } (W)^2}{2}.$$

2.7 *In vivo* fluorescence imaging

For using fluorescence microscopy *in vivo*, 4T1 tumor-bearing animals were given a fluorescent dye with AQ4N@AuNCs solution (20 mg mL^{-1}, 300 μL) *via* tail vein, and 10% chloral hydrate (0.06 mL per 10 g) was injected intraperitoneally at 0, 8, 16 and 24 hours. The fluorescence images were scanned by IVIS Lumina Series III. Before fluorescence imaging, the hair on the back of each mouse was pre-shaved to prevent hair from interfering with imaging. Following the scan, mice were sacrificed while tumor tissues and important organs, such as the heart, liver, spleen, lung, and kidney, were gathered for *ex vivo* fluorescence imaging.

2.8 *In vivo* synergistic therapy

The mice having 4T1 tumors were randomly subdivided into four groups ($n = 5$) for *in vivo* therapy acting in synergism, namely saline, saline + RT, RGDfC-AuNCs + RT, and AQ4N@AuNCs + RT groups. Animal models were given saline (300 μL), RGDfC-AuNCs solution (20 mg mL^{-1}, 300 μL) and AQ4N@AuNCs solution (20 mg mL^{-1}, 300 μL) *via* tail vein. Eight hours after injection, saline + RT, RGDfC-AuNCs + RT, and AQ4N@AuNCs + RT groups were irradiated with 8 Gy X-ray by Varian linear accelerator, and the mice without any treatment

were used as blank control. Subsequently, all mice were housed under the same conditions, and every other day, the mice were weighed, and the length (L) and width (W) of the tumors were measured. On day 14, the mice were executed, blood, tumor samples, and essential organs were gathered, and tumor samples were cleansed and weighed with normal saline. Hematological analysis, blood chemistry analysis, hematoxylin and eosin (H&E) staining, cleaved-caspase 3 and gamma-H2AX immunohistochemical staining were used to evaluate tissue-level biocompatibility and synergistic therapeutic efficacy after AQ4N@AuNCs treatment. The calculation formula of tumor growth inhibition rate is as follows:

$$\text{tumor growth inhibition rate } (\%) = \left(1 - \text{mean tumor weight of}\frac{\text{treatment group}}{\text{control group}}\right) \times 100.$$

3. Results

3.1 Synthesis and characterization of AQ4N@AuNCs

Fluorescent RGDfC-AuNCs were prepared by biomineralization method using cRGDfC peptide containing RGD sequence as a template. Next, AQ4N@AuNCs were successfully prepared by loading the hypoxia-activated prodrug AQ4N with RGDfC-AuNCs as a carrier (Fig. 2a). As depicted in Fig. 2c, RGDfC-AuNCs have a broad absorption band between 300 and 500 nm and a smaller absorption peak at 390 nm, AQ4N has a characteristic absorption peak at 610 nm, while AQ4N@AuNCs have absorption at 390 and 610 nm peaks, thus demonstrating the successful loading of AQ4N. The prepared RGDfC-AuNCs and AQ4N@AuNCs were pale yellow and blue in solution, respectively, while excitation peaks at 367 nm and emission peaks at 657 nm (Fig. 2d), and had excellent fluorescence properties *in vitro* (Fig. 3a and b). As shown in Fig. 2e and f, the hydrated particle sizes of AQ4N@AuNCs were 5.67 nm, and zeta potentials of AuNCs, AQ4N, and AQ4N@AuNCs were −5.20, +2.15 and −3.49 mV, accordingly. The hydrated particle size and zeta potential of AQ4N@AuNCs stored at 4 °C did not change significantly within 30 days, indicating the good stability of AQ4N@AuNCs (Fig. 2g). In the transmission electron microscopy (TEM) photos, RGDfC-AuNCs and AQ4N@AuNCs have a nearly spherical shape, relatively uniform particle size, and good dispersion (Fig. 2b). After loading AQ4N, the shape and particle size did not change significantly, indicating that the loading of AQ4N did not destroy the structure of AuNCs. According to the standard curve of AQ4N concentration *versus*

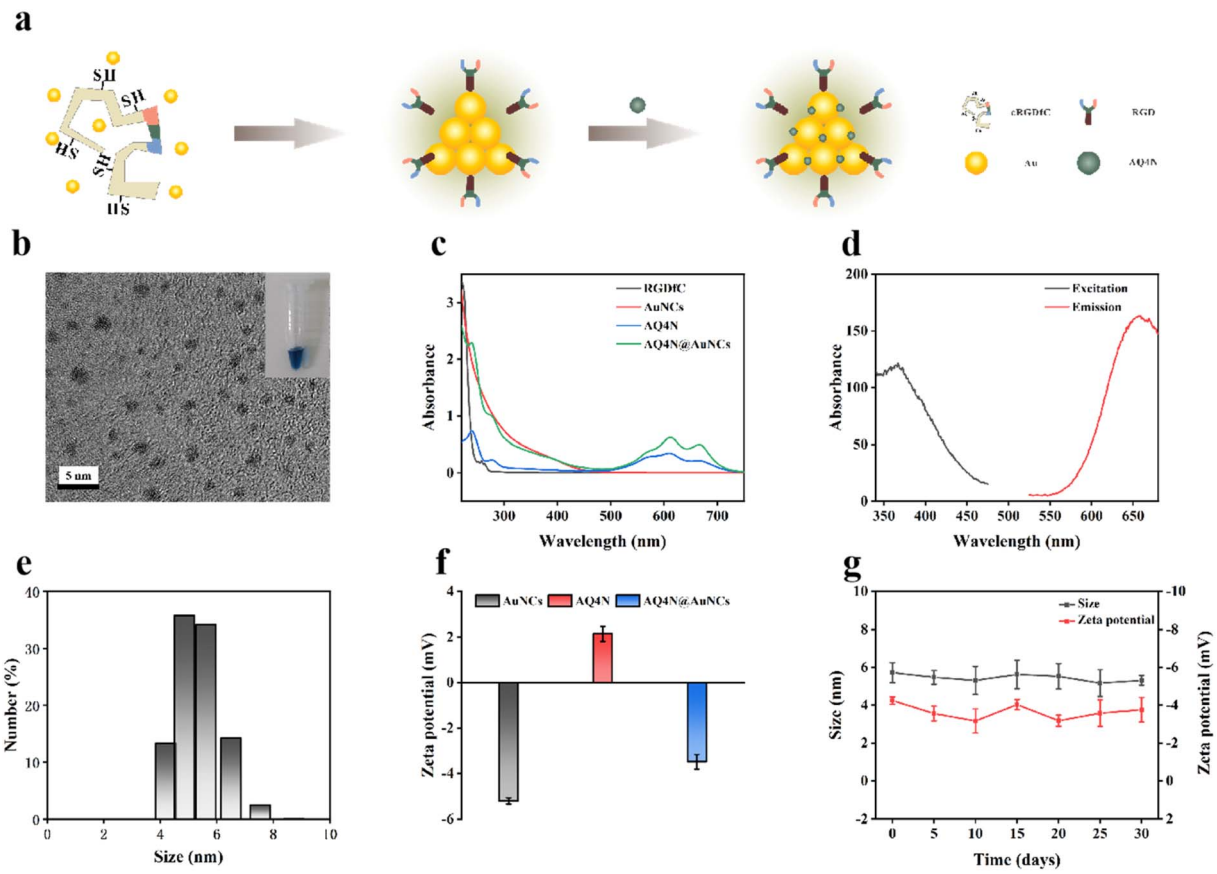

Fig. 2 Synthesis and characterization of AQ4N@AuNCs. (a) Schematic diagram of synthesis; (b) TEM images and physical photographs; (c) UV-Vis absorption spectra; (d) fluorescence excitation and emission spectra (excitation 367 nm, emission 657 nm); (e) hydrated particle size, (f) zeta potential and (g) stability at 4 °C storage for 30 days (aqueous solution, 25 °C).

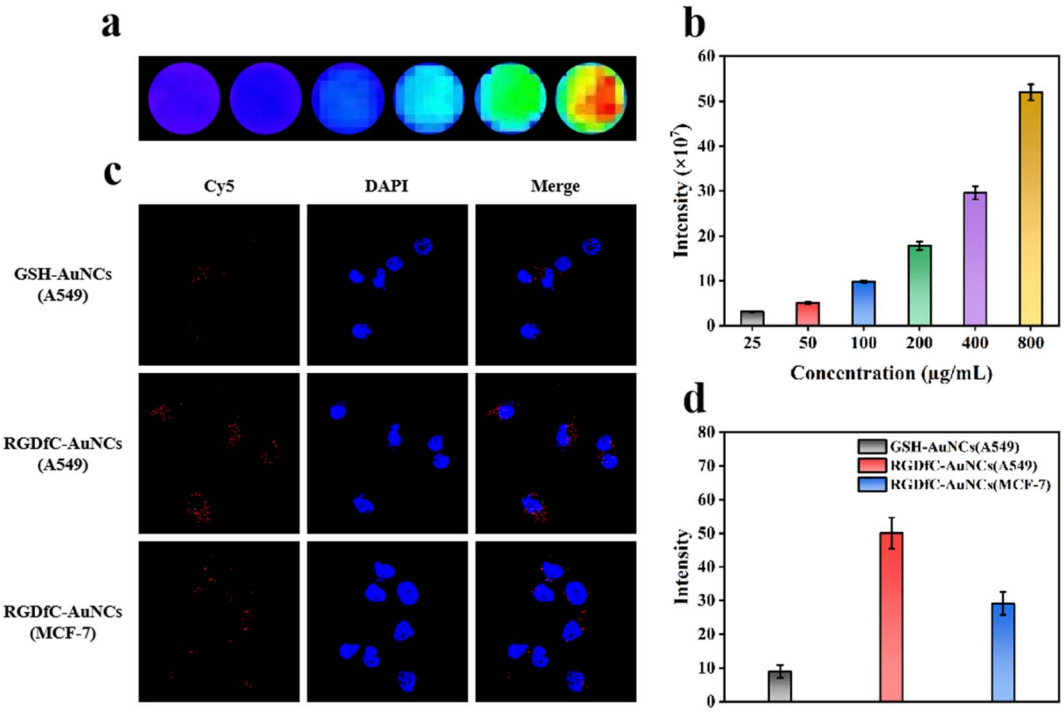

Fig. 3 *In vitro* fluorescence imaging performance and specific targeting ability. (a) *In vitro* fluorescence imaging and (b) quantitative fluorescence signal intensity (excitation 430 nm, emission 707 nm); (c) cellular uptake of GSH-AuNCs or RGDfC-AuNCs in A549 or MCF-7 cells as observed by CLSM, and (d) quantitative fluorescence signal intensity (excitation 649 nm, emission 669 nm).

absorbance, the drug loading rate of AQ4N was 14.97% (Fig. S1†).

3.2 *In vitro* cytotoxicity of AQ4N@AuNCs

We evaluated the cytotoxicity of AQ4N@AuNCs in 4T1 cells before *in vitro* and *in vivo* applications. The cell viability of 4T1 cells treated with AQ4N@AuNC was detected by CCK8 assay. The cell viability of 4T1 cells showed no significant decrease within the tested concentration spectrum after being exposed to different concentrations of AQ4N@AuNCs for a period of 24 hours; in fact, the cell vitality of 4T1 cells remained above 90% even at great concentrations like 800 μg mL^{-1} (Fig. 4a). The results showed that AQ4N@AuNCs had good biocompatibility at the cellular level.

3.3 *In vitro* cellular uptake of AQ4N@AuNCs

High cellular uptake is a prerequisite for drug release into cells leading to appropriate treatment for the tumor. To evaluate the targeting ability of AQ4N@AuNCs, we selected integrin $\alpha_v\beta_3$ receptor-positive cells, including A549 cells with high receptor expression and MCF-7 cells with low receptor expression, as cell models. We chose glutathione as a template to prepare GSH-AuNCs as a control group. For visualisation, GSH-AuNCs and RGDfC-AuNCs were labelled with the fluorescent dye Cy5 and

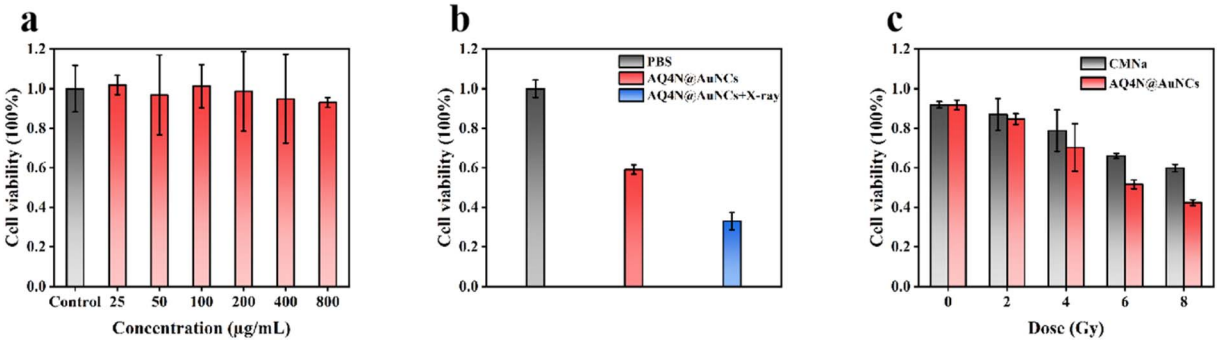

Fig. 4 Cytotoxicity and *in vitro* synergistic treatment effects of AQ4N@AuNCs. (a) Cell viability of 4T1 cells treated with different concentrations of AQ4N@AuNCs for 24 hours; (b) cell viability of 4T1 cells treated with AQ4N@AuNCs under radiation or non-radiation conditions after hypoxic pretreatment; (c) comparison of the radiosensitizing effects of AQ4N@AuNCs and CMNa at different radiation doses.

monitored by CLSM. As shown in Fig. 4c and d, only trace amounts of red fluorescence could be observed after treatment of A549 cells with GSH-AuNCs due to the lack of targeting RGD sequences, indicating relatively little accumulation. In contrast, stronger red fluorescence was observed in A549, and MCF-7 cells were applied with RGDfC-AuNCs, indicating more accumulation. Furthermore, stronger red fluorescence was observed in A549 cells with high integrin $\alpha v\beta_3$ receptor expression compared with MCF-7 cells with low integrin $\alpha_v\beta_3$ receptor expression. The results revealed that RGD sequence-containing polypeptides were an essential component in the process by which tumor cells efficiently absorb nanoparticles.

3.4 *In vitro* synergistic therapy of AQ4N@AuNCs

To assess the synergistic treatment effectiveness of AQ4N@AuNCs *in vitro*, after hypoxic pretreatment with $CoCl_2$, 4T1 cells treated with AQ4N@AuNCs were divided into AQ4N@AuNCs and AQ4N@AuNCs + X-ray group, with the addition of PBS as the blank control group. As shown in Fig. 4b, the cell survival rates were 59.03% and 32.92% for the AQ4N@AuNCs and AQ4N@AuNCs + X-ray group, respectively. The core of RGDfC-AuNCs consists of multiple gold atoms, which can generate more reactive oxygen species (ROS) in enriched regions within the tumor after X-ray irradiation, thereby enhancing the killing of normoxic tumor cells. AQ4N can be reduced to cytotoxic AQ4 under hypoxic conditions, thereby selectively killing hypoxic tumor cells. Therefore, the combined application of RGDfC-AuNCs and AQ4N can further improve the anti-tumor effect. To evaluate the radiosensitizing effect of AQ4N@AuNCs, we detected the cell viability of 4T1 cells treated with AQ4N@AuNCs (800 μg mL^{-1}) under various X-ray radiation doses (0, 2, 4, 6, and 8 Gy), treated with PBS and CMNa (clinical radiosensitizer, 800 μg mL^{-1}) as a control group. As expected, 4T1 cells treated with AQ4N@AuNCs exhibited the most efficient apoptosis. As shown in Fig. 4c, the cell viability after CMNa treatment was 59.87% at the radiation dosage of 8 Gy, while the radiation effect was greatly amplified by AQ4N@AuNCs treatment, which resulted in a viability reduction of the cells to 42.37%. The experiment revealed that AQ4N@AuNCs displayed radiosensitization activities that were either equivalent to or even better than those of CMNa.

3.5 *In vivo* fluorescence imaging

Dynamic monitoring of tumor treatment effect is essential to determine treatment efficacy, detect complications, and guide long-term treatment. Therefore, we investigated the fluorescence imaging performance of AQ4N@AuNCs *in vivo* to guarantee that a significant amount of imaging contrast agents will concentrate at tumor locations. Following the administration of AQ4N@AuNCs through i.v, 4T1 tumor-bearing mice were examined at 0 (control), 8, 16, and 24 hours after injection, respectively. As shown in Fig. 5a and b, fluorescence imaging results demonstrated a steady increase over time in fluorescence intensity at the tumor site, peaked at 8 hours, exhibited long-term tumor retention, and gradually decreased after 16 hours. Both the enhanced permeability and retention (EPR) action and the specific targeting action are connected and provided by AQ4N@AuNCs. The biodistribution of AQ4N@AuNCs was investigated *via ex vivo* fluorescence imaging of tumors and main vital organs (heart, liver, spleen, lung, and kidney). *Ex vivo* fluorescence imaging illustrated a significant concentration at tumor location 8 hours after injection, which was matched with *in vivo* fluorescence imaging (Fig. 5c). Furthermore, the organs of the reticuloendothelial system (RES) (liver and spleen) were only responsible for the clearance of a small portion of AQ4N@AuNCs, and the kidney was the primary excretory organ responsible for their elimination. This is consistent with previous reports that nanoparticles of an ultrasmall size can be eliminated from the body by the kidneys, but they can also be partially absorbed and broken down by the liver and spleen.[37,38]

3.6 *In vivo* synergistic therapy

To evaluate the efficacy of synergistic therapy *in vivo*, mice models with a 4T1 tumor, which was constructed for research on tumor treatment *in vivo*, were constructed. Mice having 4T1 tumors were randomly separated into four groups (each $n = 5$), namely saline, saline + RT, RGDfC-AuNCs + RT, and AQ4N@AuNCs + RT groups. The Fig. 6a shows that saline + RT and RGDfC-AuNCs + RT groups showed moderate tumor growth inhibition, indicating that the therapeutic effect of single radiotherapy was limited, while synergistic treatment of AQ4N@AuNCs + RT group showed obvious inhibition of tumor

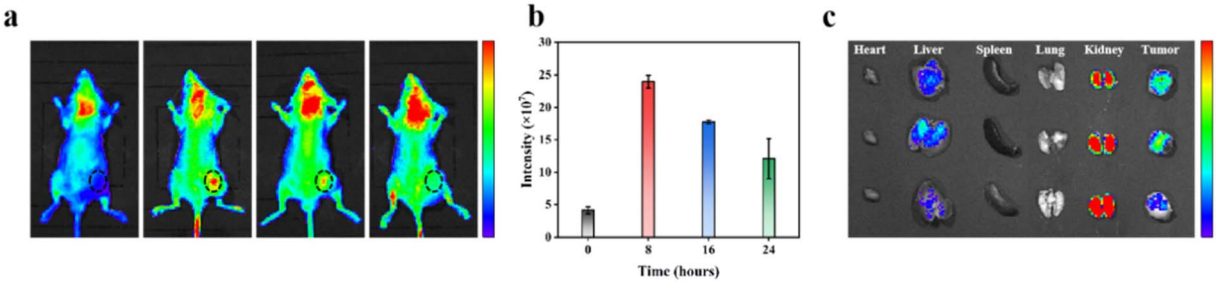

Fig. 5 *In vivo* targeted fluorescence imaging of AQ4N@AuNCs. (a) *In vivo* time-dependent fluorescence images and (b) quantitative fluorescence signal intensity after intravenous injection of AQ4N@AuNCs; (c) time-dependent *ex vivo* fluorescence images of vital organs and tumors in mice (8, 16 and 24 hours respectively). The excitation and emission wavelengths were 430 nm and 707 nm respectively.

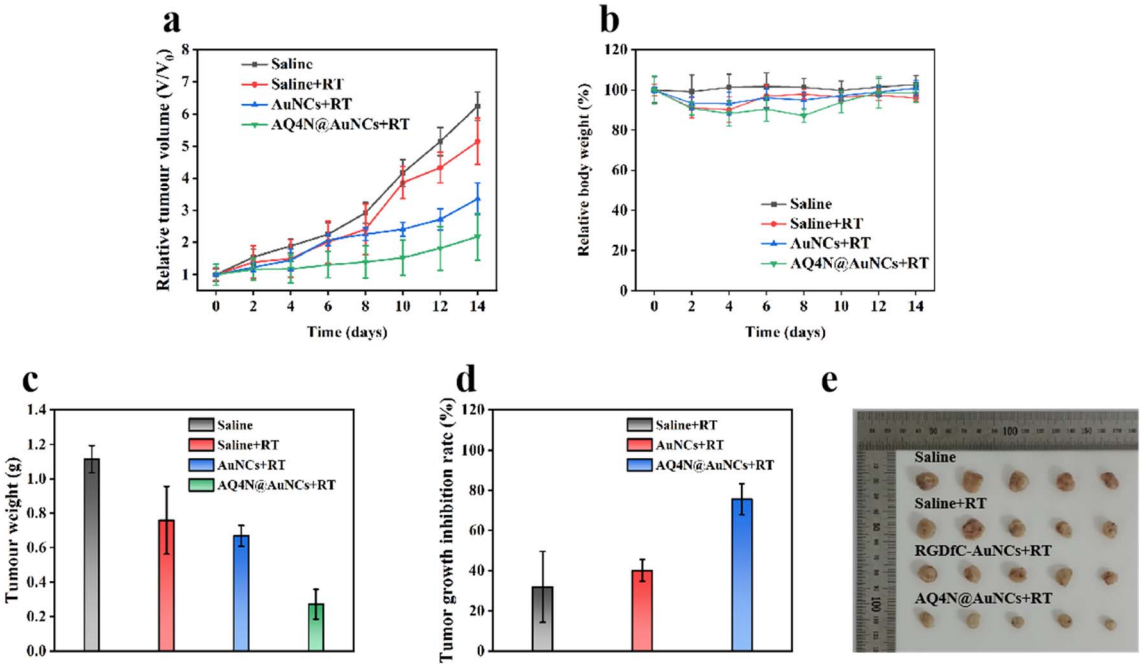

Fig. 6 *In vivo* synergistic treatment effect of AQ4N@AuNCs in 4T1 tumor-bearing mice. (a) Relative tumor volume; (b) relative body weight; (c) tumor weight; (d) tumor growth inhibition rate; (e) tumor *ex vivo* photographs.

growth. After 14 day treatment, the tumors of each group were gathered, imaged, and weighed (Fig. 6c and e). The tumor growth inhibition rate was determined using the tumor weight as the basis for the calculation. The Fig. 6d shows that the synergistic therapy with AQ4N@AuNCs significantly suppressed the growth of the tumor, and the tumor growth inhibition rate was 75.56%, significantly higher than that of another group (31.89% in saline + RT group and 40.02% in RGDfC-AuNCs + RT group). In addition, the mice's body weight in all groups was significantly the same during the treatment period and only slightly decreased after radiotherapy, indicating that the systemic toxicity of AQ4N@AuNCs is negligible (Fig. 6b). The *in vivo* biocompatibility of AQ4N@AuNCs was evaluated by comparing with the results of hematology analysis, blood

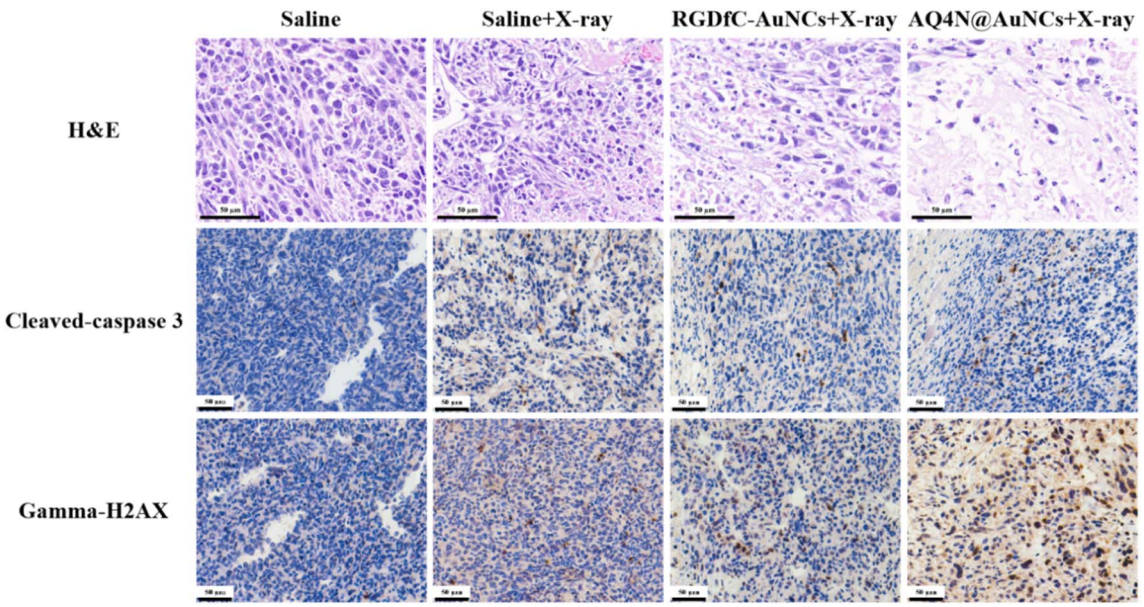

Fig. 7 H&E staining images and immunohistochemical images of tumor sections from mice in different treatment groups. First row: H&E stained images; second row: cleaved-caspase 3 immunohistochemistry images; third row: gamma-H2AX immunohistochemistry images.

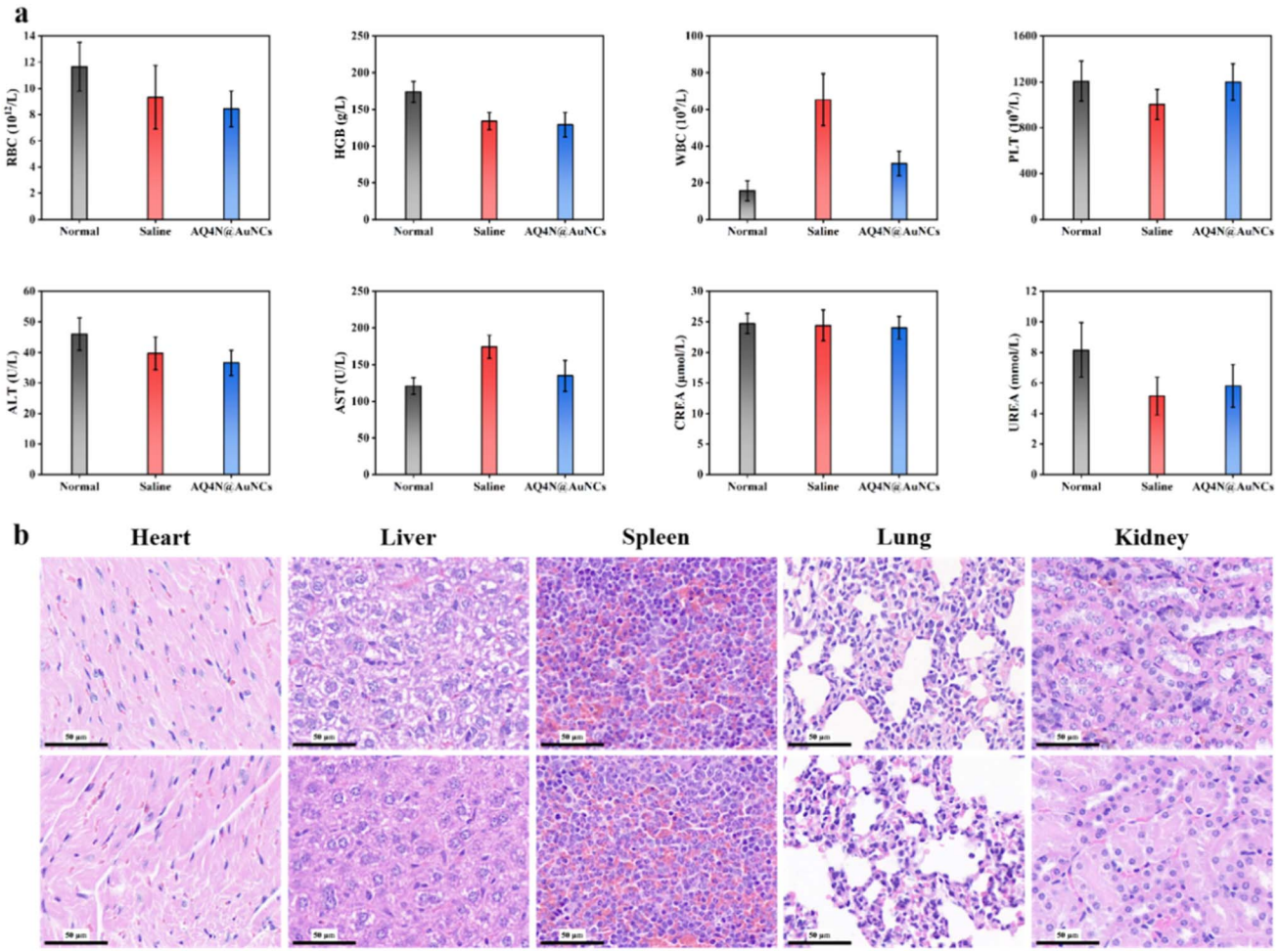

Fig. 8 *In vivo* biocompatibility of AQ4N@AuNCs. (a) Hematological analysis and blood chemistry analysis; (b) H&E stained images of vital organs (including heart, liver, spleen, lung and kidney) of normal mice and experimental group mice.

chemistry analysis, and H&E staining of vital organs in normal mice. The study findings revealed that the mice in the experimental group exhibited only a mild inflammatory reaction, no significant differences between the experimental mice and the normal mice in terms of other blood metrics, and no noticeable physiological or morphological changes in the primary organs of the mice (Fig. 8a and b). The antitumor efficacy of AQ4N@AuNCs + RT group was further analyzed by H&E and immunohistochemical staining (Fig. 7). As expected, H&E staining of tumor tissue in AQ4N@AuNCs + RT group showed more pronounced necrosis and nucleolysis compared with the control group. Cleaved-caspase 3 staining and gamma-H2AX staining revealed that apoptosis and DNA damage in AQ4N@AuNCs + RT group were greater than in the control group.

4. Conclusion

To overcome the radiation resistance induced by tumor hypoxia and make up for the limitation of single radiotherapy, gold nanoclusters were prepared by biomineralization method with cRGDfC peptide as a template and then loaded with hypoxia-activated prodrugs to prepare multifunctional nanoprobes. Surface-coated RGD sequences can enhance the specific binding of nanoprobes to integrin receptor-positive tumor cells and tumor neovascular endothelial cells, increasing accumulation in tumor tissues. AuNCs with unique structure and ultra-small size can be applied as fluorescent imaging agents and radiosensitizers. AQ4N is a novel bioreductive drug that can be reduced to cytotoxic AQ4 under hypoxic conditions, thereby selectively killing tumor hypoxic cells. The designed nanoprobes have ultra-small size, high selectivity for integrin $\alpha_v\beta_3$ receptor-positive tumor cells and tumor neovascular endothelial cells, and excellent fluorescence imaging performance. *In vitro* and *in vivo* experimental procedures demonstrate that the surface-coated designed nanoprobes have excellent biocompatibility, efficient radiosensitization effect, and anti-tumor efficacy at cell and tissue levels. The combined application of radiotherapy and hypoxia-activated therapy can suppress tumor progression and improve the efficacy of tumor radiotherapy, providing a new idea for developing the combined application of multiple therapeutic methods.

Conflicts of interest

There are no conflicts to declare.

References

1 J. M. Brown and A. J. Giaccia, The unique physiology of solid tumors: opportunities (and problems) for cancer therapy, *Cancer Res.*, 1998, **58**(7), 1408–1416.
2 G. L. Semenza, The hypoxic tumor microenvironment: a driving force for breast cancer progression, *Biochim. Biophys. Acta*, 2016, **1863**(3), 382–391.
3 M. A. Swartz, N. Iida, E. W. Roberts, S. Sangaletti, M. H. Wong, F. E. Yull, L. M. Coussens and Y. A. DeClerck, Tumor microenvironment complexity: emerging roles in cancer therapy, *Cancer Res.*, 2012, **72**(10), 2473–2480.
4 K. L. Bennewith and S. Dedhar, Targeting hypoxic tumour cells to overcome metastasis, *BMC Cancer*, 2011, **11**, 504.
5 N. C. Denko, L. A. Fontana, K. M. Hudson, P. D. Sutphin, S. Raychaudhuri, R. Altman and A. J. Giaccia, Investigating hypoxic tumor physiology through gene expression patterns, *Oncogene*, 2003, **22**(37), 5907–5914.
6 A. Giaccia, B. G. Siim and R. S. Johnson, HIF-1 as a target for drug development, *Nat. Rev. Drug Discovery*, 2003, **2**(10), 803–811.
7 R. Kumari, D. Sunil, R. S. Ningthoujam and N. A. Kumar, Azodyes as markers for tumor hypoxia imaging and therapy: an up-to-date review, *Chem.-Biol. Interact.*, 2019, **307**, 91–104.
8 H. Yang, Y. H. Geng, P. Wang, Y. T. Zhou, H. Yang, Y. F. Huo, H. Q. Zhang, Y. Li, H. Y. He, X. X. Tian and W. G. Fang, Extracellular ATP promotes breast cancer invasion and epithelial-mesenchymal transition *via* hypoxia-inducible factor 2alpha signaling, *Cancer Sci.*, 2019, **110**(8), 2456–2470.
9 Z. Lu, J. Gao, C. Fang, Y. Zhou, X. Li and G. Han, Porous Pt Nanospheres Incorporated with GOx to Enable Synergistic Oxygen-Inductive Starvation/Electrodynamic Tumor Therapy, *Adv. Sci.*, 2020, **7**(17), 2001223.
10 X. Yang, Y. Yang, F. Gao, J. J. Wei, C. G. Qian and M. J. Sun, Biomimetic Hybrid Nanozymes with Self-Supplied H(+) and Accelerated O_2 Generation for Enhanced Starvation and Photodynamic Therapy against Hypoxic Tumors, *Nano Lett.*, 2019, **19**(7), 4334–4342.
11 L. Feng, L. Cheng, Z. Dong, D. Tao, T. E. Barnhart, W. Cai, M. Chen and Z. Liu, Theranostic Liposomes with Hypoxia-Activated Prodrug to Effectively Destruct Hypoxic Tumors Post-Photodynamic Therapy, *ACS Nano*, 2017, **11**(1), 927–937.
12 Y. Wang, Y. Xie, J. Li, Z. H. Peng, Y. Sheinin, J. Zhou and D. Oupicky, Tumor-Penetrating Nanoparticles for Enhanced Anticancer Activity of Combined Photodynamic and Hypoxia-Activated Therapy, *ACS Nano*, 2017, **11**(2), 2227–2238.
13 S. P. Chawla, L. D. Cranmer, B. A. Van Tine, D. R. Reed, S. H. Okuno, J. E. Butrynski, D. R. Adkins, A. E. Hendifar, S. Kroll and K. N. Ganjoo, Phase II study of the safety and antitumor activity of the hypoxia-activated prodrug TH-302 in combination with doxorubicin in patients with advanced soft tissue sarcoma, *J. Clin. Oncol.*, 2014, **32**(29), 3299–3306.
14 W. A. Denny, Hypoxia-activated prodrugs in cancer therapy: progress to the clinic, *Future Oncol.*, 2010, **6**(3), 419–428.
15 K. N. Ganjoo, L. D. Cranmer, J. E. Butrynski, D. Rushing, D. Adkins, S. H. Okuno, G. Lorente, S. Kroll, V. K. Langmuir and S. P. Chawla, A phase I study of the safety and pharmacokinetics of the hypoxia-activated prodrug TH-302 in combination with doxorubicin in patients with advanced soft tissue sarcoma, *Oncology*, 2011, **80**(1–2), 50–56.
16 G. J. Weiss, J. R. Infante, E. G. Chiorean, M. J. Borad, J. C. Bendell, J. R. Molina, R. Tibes, R. K. Ramanathan, K. Lewandowski, S. F. Jones, M. E. Lacouture, V. K. Langmuir, H. Lee, S. Kroll and H. A. 3rd Burris, Phase 1 study of the safety, tolerability, and pharmacokinetics of TH-302, a hypoxia-activated prodrug, in patients with advanced solid malignancies, *Clin. Cancer Res.*, 2011, **17**(9), 2997–3004.
17 S. Clement, J. M. Campbell, W. Deng, A. Guller, S. Nisar, G. Liu, B. C. Wilson and E. M. Goldys, Mechanisms for Tuning Engineered Nanomaterials to Enhance Radiation Therapy of Cancer, *Adv. Sci.*, 2020, **7**(24), 2003584.
18 C. Klein, I. Dokic, A. Mairani, S. Mein, S. Brons, P. Haring, T. Haberer, O. Jakel, A. Zimmermann, F. Zenke, A. Blaukat, J. Debus and A. Abdollahi, Overcoming hypoxia-induced tumor radioresistance in non-small cell lung cancer by targeting DNA-dependent protein kinase in combination with carbon ion irradiation, *Radiat. Oncol.*, 2017, **12**(1), 208.
19 X. Li, J. Li, C. Li, Q. Guo, M. Wu, L. Su, Y. Dou, X. Wu, Z. Xiao and X. Zhang, Aminopeptidase N-targeting nanomolecule-assisted delivery of VEGF siRNA to potentiate antitumour therapy by suppressing tumour revascularization and enhancing radiation response, *J. Mater. Chem. B*, 2021, **9**(36), 7530–7543.
20 Y. Yong, C. Zhang, Z. Gu, J. Du, Z. Guo, X. Dong, J. Xie, G. Zhang, X. Liu and Y. Zhao, Polyoxometalate-Based Radiosensitization Platform for Treating Hypoxic Tumors by Attenuating Radioresistance and Enhancing Radiation Response, *ACS Nano*, 2017, **11**(7), 7164–7176.
21 R. Song, S. Peng, Q. Lin, M. Luo, H. Y. Chung, Y. Zhang and S. Yao, pH-Responsive Oxygen Nanobubbles for Spontaneous Oxygen Delivery in Hypoxic Tumors, *Langmuir*, 2019, **35**(31), 10166–10172.
22 L. Y. Chen, C. W. Wang, Z. Yuan and H. T. Chang, Fluorescent gold nanoclusters: recent advances in sensing and imaging, *Anal. Chem.*, 2015, **87**(1), 216–229.
23 C. Fan, S. Zhai, W. Hu, S. Chi, D. Song and Z. Liu, Gold nanoclusters as a GSH activated mitochondrial targeting photosensitizer for efficient treatment of malignant tumors, *RSC Adv.*, 2021, **11**(35), 21384–21389.
24 J. Xie, Y. Zheng and J. Y. Ying, Protein-directed synthesis of highly fluorescent gold nanoclusters, *J. Am. Chem. Soc.*, 2009, **131**(3), 888–889.

25 S. Xu, Y. Duan and B. Liu, Precise Molecular Design for High-Performance Luminogens with Aggregation-Induced Emission, *Adv. Mater.*, 2020, **32**(1), e1903530.
26 B. Yang, Y. Chen and J. Shi, Reactive Oxygen Species (ROS)-Based Nanomedicine, *Chem. Rev.*, 2019, **119**(8), 4881–4985.
27 G. Liang, X. Jin, S. Zhang and D. Xing, RGD peptide-modified fluorescent gold nanoclusters as highly efficient tumor-targeted radiotherapy sensitizers, *Biomaterials*, 2017, **144**, 95–104.
28 M. Hossain and M. Su, Nanoparticle location and material dependent dose enhancement in X-ray radiation therapy, *J. Phys. Chem. C*, 2012, **116**(43), 23047–23052.
29 S. J. McMahon, W. B. Hyland, M. F. Muir, J. A. Coulter, S. Jain, K. T. Butterworth, G. Schettino, G. R. Dickson, A. R. Hounsell, J. M. O'Sullivan, K. M. Prise, D. G. Hirst and F. J. Currell, Biological consequences of nanoscale energy deposition near irradiated heavy atom nanoparticles, *Sci. Rep.*, 2011, **1**, 18.
30 J. Liu, M. Yu, C. Zhou, S. Yang, X. Ning and J. Zheng, Passive tumor targeting of renal-clearable luminescent gold nanoparticles: long tumor retention and fast normal tissue clearance, *J. Am. Chem. Soc.*, 2013, **135**(13), 4978–4981.
31 C. Zhou, G. Hao, P. Thomas, J. Liu, M. Yu, S. Sun, O. K. Oz, X. Sun and J. Zheng, Near-infrared emitting radioactive gold nanoparticles with molecular pharmacokinetics, *Angew. Chem., Int. Ed.*, 2012, **51**(40), 10118–10122.
32 R. O. Hynes, Integrins: bidirectional, allosteric signaling machines, *Cell*, 2002, **110**(6), 673–687.
33 P. C. Brooks, R. A. Clark and D. A. Cheresh, Requirement of vascular integrin alpha v beta 3 for angiogenesis, *Science*, 1994, **264**(5158), 569–571.
34 M. Alipour, M. Baneshi, S. Hosseinkhani, R. Mahmoudi, A. Jabari Arabzadeh, M. Akrami, J. Mehrzad and H. Bardania, Recent progress in biomedical applications of RGD-based ligand: from precise cancer theranostics to biomaterial engineering: a systematic review, *J. Biomed. Mater. Res., Part A*, 2020, **108**(4), 839–850.
35 A. Mousavizadeh, A. Jabbari, M. Akrami and H. Bardania, Cell targeting peptides as smart ligands for targeting of therapeutic or diagnostic agents: a systematic review, *Colloids Surf., B*, 2017, **158**, 507–517.
36 Y. Wang, Y. Cui, Y. Zhao, R. Liu, Z. Sun, W. Li and X. Gao, Bifunctional peptides that precisely biomineralize Au clusters and specifically stain cell nuclei, *Chem. Commun.*, 2012, **48**(6), 871–873.
37 M. Longmire, P. L. Choyke and H. Kobayashi, Clearance properties of nano-sized particles and molecules as imaging agents: considerations and caveats, *Nanomedicine*, 2008, **3**(5), 703–717.
38 K. M. Tsoi, S. A. MacParland, X. Z. Ma, V. N. Spetzler, J. Echeverri, B. Ouyang, S. M. Fadel, E. A. Sykes, N. Goldaracena, J. M. Kaths, J. B. Conneely, B. A. Alman, M. Selzner, M. A. Ostrowski, O. A. Adeyi, A. Zilman, I. D. McGilvray and W. C. Chan, Mechanism of hard-nanomaterial clearance by the liver, *Nat. Mater.*, 2016, **15**(11), 1212–1221.